

Constitutive Relations Analyses of Plastic Flow in Dual-Phase Steels to Elucidate Structure–Strength–Ductility Correlations

S. SAIMOTO,^{1,4} I.B. TIMOKHINA,² and E.V. PERELOMA³

1.—Mechanical and Materials Engineering, Queen's University, Kingston, ON K7L3N6, Canada.
2.—Centre for Material and Fibre Innovation, Deakin University, Geelong, VIC 3217, Australia.
3.—School of Mechanical, Material and Mechatronics Engineering, University of Wollongong, Wollongong, NSW 2500, Australia. 4.—e-mail: shigeo.saimoto@queensu.ca

The structure–strength characterization is typically performed by correlating the structure with x-ray, electron, or atomic imaging devices to the bulk mechanical tensile parameters of yield stress and the plastic yielding response. The problem is that structure parameters embedded in the stress–strain data cannot be revealed without an analyzable constitutive relation. New functional slip-based constitutive formulation with precise digital fitting parameters can replicate the measured data with at least two loci. Thus, this study examines the possibility of identifying the mechanical response as a result of the various microstructure components. The key parameter, the mean slip distance, can be calibrated from the initial work-hardening slope at 0.2% strain from which all the fit parameters can be determined. In this process, a newly derived friction stress is defined to separate the yield phenomenon from the plastic strains beyond yield-point elongation. This methodology has been applied to dual-phase steel specimens that resulted in excellent predictive correlations with prior structure–strength characterization. Hence, the structure–strength–ductility changes resulting from processing conditions can be more precisely surmised from mechanical testing. Thus, a method to delineate the nanostructure evolution with deformation using mesoscopic mechanical parameters has been introduced.

INTRODUCTION

Steels are material of choice for a very wide range of applications in the construction, manufacturing, and automotive industries as a result of the economic benefits of their high-volume production, recyclability, and a large spectrum of mechanical properties. Dual-phase (DP) steels are widely used in the automotive industry because of their combination of high strength and ductility resulting in car weight reduction, fuel economy, and lowered CO₂ emission.¹ These properties are a result of the microstructure comprising soft polygonal ferrite and hard martensite phases with sometimes small amounts of bainite and retained austenite.^{2,3} Knowledge of the mechanical behavior of these steels during forming operations or in service is essential. One of the earliest formal studies of plastic deformation of steel was performed by Hollomon⁴ who pragmatically proposed a power-

law relation $\sigma = K_H \varepsilon^n$, correlating tensile stress σ to tensile strain ε with material constant K_H . Since then, several constitutive equations have been developed to describe flow curves and the work-hardening behavior of single- and multiphase steels.^{5,6} Nevertheless, the analyses to quantitatively assess the mechanical behavior to identify the local deformation modes around various microstructure components as manifested by the stress–strain diagram is still inadequate, despite the unprecedented advance in microstructural characterization using modern optical, x-ray, electron, and atomic imaging devices.⁷ Recent studies by Tasan et al.^{8,9} illustrate the sophisticated applications of these techniques to simulate the grain-by-grain deformation using crystal plastic finite element method (CPFEM). Yet, the present quality-control practice to assess ductility is the pragmatic one of bending tests for specific applications.⁷ Thus, the structure–strength correlation is well documented, but the

structure–strength–ductility predictive analyses have not been elucidated. The primary reason for this status quo is attributed to the lack of a constitutive relation that can precisely replicate the plastic behavior of steel stock materials.

Recently, in the case of face-centered-cubic (fcc)^{10,11} and close-packed-hexagonal (hcp)¹² metals, a procedure to generate a predictive replicative constitutive relation has been derived and applied to unidirectional testing at various temperatures.¹¹ This constitutive relations analysis (CRA) is based on formulation of a functional relation between the energy required to form slipped areas to comply with the imposed strain and equated with the energy of the stored work. This energy balance invokes a simple annihilation factor, A , to account for the large difference between the energy expended and the stored work, as first reported by Lord Kelvin.¹³ Thus, this initial study was undertaken to explore the application of this methodology to DP steels. The as-processed DP steels manifest smooth, monotonic, work-hardening behavior typical of polycrystalline plastic behavior but, upon bake hardening (BH) at 175°C for 30 min, exhibits a yield phenomenon with a large yield-point elongation (YPE).¹⁴ This effect complicates the determination of the calibration factor for the mean slip distance λ compared with those with continuous monotonic yield evolution, and hence, a self-consistent procedure had to be devised. The validation of the microstructural interpretation from the mechanical behavior was performed by comparison with prior microstructural characterization using x-ray and transmission electron microscopy (TEM)¹⁴ as well as atom probe tomography (APT).¹⁵ In summary, the described procedure of CRA is sufficiently predictive so that it can be used as a guide to select the critical heat treatments that require more detailed characterization or validation using various electron imaging methods. Moreover, the proposed analyses have the promise of improving mechanical data characterization.

EXPERIMENTAL MATERIAL

The specimens that were tensile tested using a servo-hydraulic machine with a 100-kN load cell and appropriate extensometers have been previously described in detail together with the x-ray and TEM studies.¹⁴ The nominal strain rate used was $6 \times 10^{-4} \text{ s}^{-1}$. The mechanical data were all recorded digitally for analyses. The chemical composition of DP steel in wt.% were 0.036 C; 1.065 Si; 1.08 Mn; 0.018 Al; 0.004 Cu; 0.083 Cr; and balance Fe.

CONSTITUTIVE RELATION ANALYSIS (CRA)

The described CRA became possible upon discovering a way to calibrate the mean slip distance λ .^{10,16}

$$\lambda = \varphi b \mu^2 \partial\gamma / 2\tau \partial\tau_{T,\dot{\gamma}} \quad (1)$$

whereby the flow shear stress τ is determined from $(\sigma - \sigma_0^{\text{final}})/M$; the shear strain, $\gamma = M\varepsilon$ in which M is the Taylor factor; μ , the shear modulus; b , the Burgers vector; and φ , the calibration factor is derived from $\theta_{\text{cal}} = \partial\tau/\partial\gamma$ at 0.2% ε given as $1/\varphi = (\mu/\theta_{\text{cal}})/2\alpha$. The derived yield stress σ_0^{final} is determined by back-extrapolation. The relation for τ to the interobstacle spacing ℓ is $\tau = \alpha\mu b/\ell$ wherein α is the coefficient of obstacle strength. This definition of shear flow stress is based on the principle that shear strain does not start to occur without dislocation movement and subsequent work hardening is a result of the new obstacles it creates during this strain interval.

Using the Taylor¹⁷ slip analysis, the strain-imposed creation energy can be equated to the stored energy and balanced with factor A as a measure of the energy lost to heat. The resulting functional constitutive relation is given with fit parameters, P/A , β and C_1 from $\lambda = C_1\tau^\beta$:

$$\tau = \left[\left(\frac{P}{4A} \right) (2 + \beta) (\alpha\mu b)^2 \frac{1}{C_1 b} \right]^{1/(2+\beta)} \gamma^{1/(2+\beta)} \quad (2)$$

The fitting is carried out by examining the measured true stress, σ , and true strain, ε , using data points from near the ultimate tensile stress down toward YPE. The data set to be fitted is terminated when the monotonic increasing slope begins to decrease. After converting this truncated data set into a polynomial fit of τ and γ , two loci, β_1 and β_2 , are created in combination with the back-extrapolated σ_0^{final} and iteratively assessed to determine the optimal fit, which produces the least amount of difference between the derived curves and the original data. The final result is reconverted back into $\sigma - \varepsilon$ terms. The determined power law exponents β_1 and β_2 and their intersection point at τ_3 and γ_3 are noted. From the value of the bracket term in Eq. 2, P/A is determined wherein C_1 is derived from the $\log \lambda$ using Eq. 1 versus $\log \tau$. Note that the β values are derived from the fitting process and not from the $\log \lambda - \log \tau$ plot subsequently plotted wherein deviation occurs whenever YPE is present. The fitted parameters are β_1 , β_2 , σ_0^{final} , P/A , and C_1 . In this relation, P is a ratio (y/x) of geometrical factors derived by assuming the new segments lengths of expanding dislocations is given as $y \lambda$ and the encircling swept area as $x \lambda^2$ to produce the shear strain as function of λ . The constant C_1 is determined at $\log \tau = 0$ and for simplicity recorded as a length term omitting the stress units. The unit of the bracket term is given as $\text{MPa}^{(2+\beta)}$. Note since $1/(2 + \beta)$ is analogous to n in the Hollomon relation, the proportionality constant, K , which is equivalent to K_H , can be precisely determined for each stress–strain data set. The strain rate sensitivity is determined by plotting the \log [bracket] term versus $\log \dot{\gamma}$ resulting in the advanced Hollomon form:¹⁸

$$\sigma_\tau = \sigma - \sigma_0^{\text{final}} = K_{S-VH} \dot{\varepsilon}^m \varepsilon^{1/(2+\beta)} \quad \text{whereby } \sigma_\tau = M \tau \quad (3)$$

Table I. Derived fit parameters for dual-phase steel from standard tensile testing data
 $\tau = \left[\left(\frac{P}{4A} \right) (2 + \beta) (\alpha \mu b)^2 \frac{1}{C_1 b} \right]^{1/(2+\beta)} \gamma^{1/(2+\beta)}$, using constant input values*

Sample	σ_0^{final}	β_1	$C_1(\beta_1)$	β_2	$C_1(\beta_2)$	τ_3 (MPa)	γ_3	λ_3 (μm)
IA	451.4	0.064	2.95E-7	0.611	4.00E-8	71.9	0.215	0.431
IA-BH	117.2	3.73	4.86E-16	4.02	1.00E-16	201.3	0.297	0.196
2%-BH	183.6	4.92	1.95E-18	—	—	—	—	—
5%-BH	326.2	6.00	7.02E-20	9.09	2.00E-26	138.0	0.246	0.531
10%-BH	455.5	5.16	5.59E-17	7.89	4.00E-22	87.63	0.137	0.670

*Constant values: $\alpha = 0.3$ [18]; $\mu = 86.0$ GPa; $b = 0.2482$ nm; $1/\varphi = 201.87$; $P/A = 0.1101$.

The parameters in Eq. 2 are listed in Table I together with the inputs $1/\varphi$, μ , and α that are all determined for each tensile test. The insertion of β_1 and β_2 values in $\log \lambda$ versus $\log \tau$ plot will show some deviation especially at very low strains. The CRA has been derived in detail elsewhere¹⁰ in analyzing the volume fraction of point defects produced by deformation¹⁹ and the drag on dislocations caused by deformation debris¹¹ and its correlation with thermally activated flow processes.¹⁸ This methodology divides the stress-strain response into primarily three separate sectors: The back-extrapolation of the initial fit locus defines the friction stress σ_0^{final} and separates the yield phenomenon from the plastic flow at higher strains. The increasing flow stress τ is the work-hardening response and is separate from the intrinsic friction heat effect as a result of the movement of dislocations. Thus, Eqs. 2 and 3 pertain only to the plastic flow component and the static obstacles are encompassed in the friction stress. The σ_0^{final} is comparable to the proportional limit but for pragmatic reasons can be taken to be at 0.02% ε .

To extend CRA to diffuse necking, the uniform elongation is determined at the ultimate tensile strength (UTS) by differentiation of Eq. 3 with respect to strain, wherein:

$$\partial\sigma/\partial\varepsilon = (\sigma - \sigma_0^{\text{final}})/\varepsilon (1/(2 + \beta) + m \partial \ln \dot{\varepsilon} / \partial \ln \varepsilon)$$

Thus:

$$\varepsilon_U = [(\sigma - \sigma_0^{\text{final}})/\sigma] (1/(2 + \beta) + m \partial \ln \dot{\varepsilon} / \partial \ln \varepsilon) \quad (4)$$

It is apparent that ε_U decreases as the yield stress increases as in the case of tempered steel. For constant strain rate tests, the standard Considère form is evident whereby $\varepsilon_U = \varepsilon_{\text{max}} = 1/(2 + \beta) = n$, but for constant displacement tests of screw-driven machines, $\dot{\varepsilon}$ decreases with strain and hence for positive m , ε_U decreases. Nevertheless, as work-hardening evolves into this penultimate stage, β can increase and depending on the microstructure can undulate¹¹ leading to a prolonged diffuse neck or occasional occurrence of double necks. This effect can be characterized by:

$$\partial\varepsilon_U/\partial\beta = [(\sigma - \sigma_0^{\text{final}})/\sigma] \left\{ -1/(2 + \beta)^2 \right\} \quad (5)$$

As shown in supplementary Fig. 1b, β undulations are measurable in fcc structures as a result of nanovoid growth leading to ductile failure²⁰ but to a lesser degree in bcc structures because deformation debris resulting from vacancy coalescence is much reduced in bcc metals.²¹ Nevertheless, it is evident that specimens with continuous increasing β will manifest a lower ε_U (see the supplementary text).

The predictive capability of the Saimoto-Van Houtte constitutive relation¹⁰ as illustrated by its application to the Considère relation in Eq. 4 suggests that other characterizations of the microstructure may be possible. In the case of modeled, randomly dispersed nanoparticles in pure metal matrix by Ashby,²² the mean slip distance λ^G associated with generation of geometrically necessary prismatic loops (GNPLs) for nonshearable particles is given by r_p/f_p , wherein r and f refer to the radius and volume fraction of the particles, respectively. In this situation, λ^G is constant and predicts that $\log \lambda$ versus $\log \tau$ plot will manifest a horizontal section. To express this effect in constituent form, Eq. 2 can be rewritten as Eq. 6 and differentiated with respect to γ to result in Eq. 7:

$$\tau^2 = \left[\left(\frac{P}{4A} \right) (2 + \beta) (\alpha \mu)^2 b \right] \gamma / \lambda^G \quad (6)$$

$$\partial\tau/\partial\gamma = \left[\left(\frac{P}{4A} \right) (2 + \beta) (\alpha \mu)^2 b \right] \frac{1}{2\lambda^G\tau} \quad (7)$$

Thus, if geometrically necessary loops are produced at yield, the initial section of the $\partial\tau/\partial\gamma$ versus $1/\tau$ plot should become linear, that is, constant λ to result in parabolic hardening. Such an observation has been found in trial analysis of quenched and tempered steel of Hollomon data,²³ and application of this methodology to the present samples will be assessed to examine whether the role of martensite is that of a shearable or unsharable particle.

The application of CRA is phenomenological in that it begins the analyses with a polynomial fitted locus, but this locus is replaced to conform to the

slip-based functional constitutive relation. This process assures that the back and forward extrapolations would be model based. In this way, CRA attempts to decipher the work-hardening contributions of the microstructure components. On the other hand, other past models have devised a procedure to simulate the bulk relation by assuming that the load-carrying stresses can be partitioned into various strengthening mechanisms, the sum of which is compared with the measured data. The present method reverses this procedure whereby the precise plastic response is analyzed to assess whether the monotonic increase in flow stress is a result of obstacles created by additional geometrically necessary dislocation (GND) such as rotated lattice structures, GNPL, or incidental random dislocation density because the strength of the response depends on the obstacle type and configuration. The yield phenomenon is attributed to solute solution and nanoparticle distribution or segregation. In future work, the determination of strain rate sensitivity using the plot of inverse activation volume versus applied stress^{18,21} would supplement this analysis. The recent studies on DP steels attempt to simulate quasi-statically the evolution of the microstructure using CPFEM of representative elemental volumes by nanohardness testing to correlate to bulk data.^{8,9} The solid solution and nanoparticle effects are inherent to the hardness results. In future studies, both types of analyses can be carried out on the same start material for comparison.

RESULTS

For the sake of clarity, the data analyses will be initially performed for the as-quenched, as-received DP steel (IA), which does not manifest a yield point, and hence, the reduced figures follow similarly to those of pure metals and natural-aged Al alloys. On the other hand, the prestrained and aged specimens (BH, designations used in Table I correspond to prior work)¹⁴ manifest a large YPE and back-extrapolation is required to separate the yield phenomenon to define σ_0^{final} . Nonetheless, the plastic flow characteristics at high strains were similar to that of IA. The validity of the procedures used can only be assessed by postexamination of the results in the Discussion section.

CRA of As-Processed Specimen IA

In Fig. 1a, $\log \lambda$ versus $\log \tau$ delineates the curve fitting procedure for IA. After selection of φ as described, λ as derived point by point from the digitized data are plotted and the optimum fitting power-law exponents β_1 and β_2 are also depicted together with $\log 1/\ell$ locus, which is referenced as $\log \alpha \mu b$ at $\log \tau = 0$. As noted, the parameterized lines do not overlap the measured $\log \lambda$ versus $\log \tau$ as a result of the fit process being applied to the total plastic behavior rather than local segments,

but the exaggerated difference occurs at very low strains where displacement recording tends to be jerky. The locus denoted $1/\ell$ is derived from the relation $\tau = \alpha \mu b/\ell$ depicting linear hardening. Using the fit parameters listed in Table I, the modeled τ - γ (Fig. 1b) and σ - ε curves (Fig. 1c) are shown comparing them to the measured stress-strain data. Note that as a result of the extended diffuse neck region, the true stress-true plastic strain calculations are carried beyond its true applicability instead of reverting to engineering stress and strain. Yet, the fits are carried out only to maximum σ . The σ_0^{final} value was 451.43 MPa and was taken to correspond to the proportional limit set at 0.02% ε . Thus, the inference is that the increasing τ with strain is a result of the increase in obstacles in terms of dislocation density and/or dislocation loops. The analysis for the generation of GNPL in Eq. 7 indicates that a region of constant λ should be observed that is absent in Fig. 1a and a locus pattern typically characteristic of single-phase alloys is found suggesting that the steel with polygonal ferrite comprises 75% of the microstructure¹⁴ and is behaving as a single phase without nonshearable nanoparticles. Thus, at first approximation, the applied stress is shared by both martensite and ferrite but only the ferrite contributes to plastic flow. Nonetheless, shearable GP zone type solute clusters have been shown to manifest behavior similar to single-phase alloys,²⁰ and hence, solutes and solute clusters may be embedded in the ferrite.

Another issue arises in considering the flow stress of a microstructure, which comprised 75% of ductile polygonal ferrite and 25% of martensite.¹⁴ Assuming that the martensite does not plastically deform, a first-order approximation ignoring load transfer effects is to presume that it must carry 25% of the load at all levels, that is, 25% σ . Thus, converting to shear stresses, $\sigma = \sigma_0^{\text{final}} + \sigma_{\text{mart}} + \sigma_{\text{disln}}$ using $\tau = (\sigma - \sigma_0^{\text{final}})/M$, $\tau = f_{\text{mart}} \tau_{\text{mart}} + f_{\text{disln}} (\tau_{\text{disln}} + \tau_{\text{GNPL}})$ and hence $\tau - 0.25 \tau = 0.75 (\tau_{\text{disln}} + \tau_{\text{GNPL}})$ resulting in $\tau = (\tau_{\text{disln}} + \tau_{\text{GNPL}})$. To assess this prediction, the correlation of the flow stress to the dislocation density can be used. The previous empirical hypothesis of correlating the measured mean dislocation density to the mean flow stress has recently been validated by showing that the local activation work, depicted by subscript L , $\tau_L v_L = \tau v$ using mean values for the flow stress and the activation volume,¹⁸ that is, the internal stresses do not affect the mean dislocation density determinations. Using this concept, the dislocation densities at the various prestrain locations for specimen IA can be calculated. Table II compares the values derived from $(\sigma - \sigma_0^{\text{final}})/M$ to those from TEM measured ones. Note the densities ρ derived from shear stress are intersection densities, which is $1/2$ that of total length ρ_t determined from TEM. Although the available data set is only two, the comparison of the measured densities to those calculated varies by

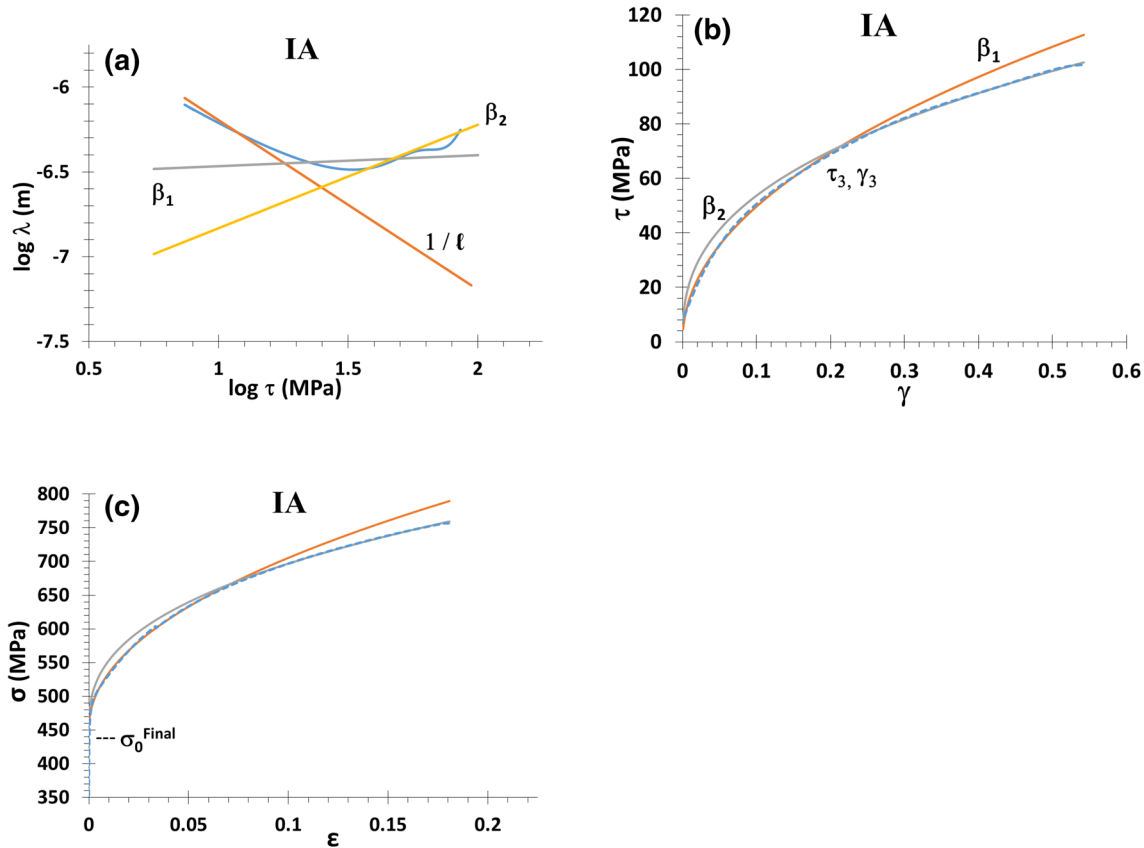


Fig. 1. (a) $\log \lambda$ versus $\log \tau$ plot showing the two parameters derived from the two-fit process and its deviation at low strains, outlined by the linear hardening locus ($1/\ell$). (b) The fitted flow stress τ versus shear strain γ compared to derived data set (dashed line) with the intersection of the loci shown. Note the undulations at high strains. (c) The original data set compared with the fitted loci showing σ_0^{final} .

<50%. Thus the choice of $\alpha = 0.3$ suggested by Delince et al.²⁴ seems reasonable because this factor is squared to derive the densities. Hence, the presumption that martensite undergoes much less shape change than the ferrite portion seems applicable resulting in $\tau = (\tau_{\text{disln}} + \tau_{\text{GNPL}})$. Furthermore, because the intersection of loops requires a much reduced α compared to dislocations,^{18,25} τ_{GNPL} must be negligible. Thus, the implication is that dislocation density is higher than that for single-phase ferrite as a result of martensite-induced load transfer stresses. To further assess the microstructure change using the CRA, the effect of bake hardening at 175°C for 30 min is examined.

CRA of As-Processed Specimens Tempered at Paint-Bake Temperatures (BH)

Upon BH, a large YPE occurs past the 0.2% strain where the calibration of φ is performed and a distinct lower yield point σ_{LYP} is observed. Hence, after many trials to attest for self-consistency, it was concluded that the same φ value as that for the as-quenched IA will be used. The reason is that mean slip distance is a performance parameter for moving dislocations, and hence, beyond YPE, the generation and annihilation mechanisms will be similar even after BH because

large changes to the microstructure will not occur except for possible formation of shearable nanocarbide particles. Using the back-extrapolated curve at 0.2% ϵ gives very similar results. Figure 2a shows the resulting $\log \lambda$ versus $\log \tau$ beyond YPE in which β_1 and β_2 are nearly identical with the accompanying σ - ϵ fits depicted in Fig. 2b. As a result of YPE, the minimum λ did not occur for IA-BH and others with BH after prestrains. In Table II, these specimens are identified as % engineering strain-BH and YPE is given in engineering strain, ϵ . All stress values are in terms of true stress. The $\log \lambda$ versus $\log \tau$ and the fitted σ - ϵ loci are presented in Fig. 3 for 2-BH, 5-BH, and 10-BH. Furthermore, in Table II, the accompanying σ_0^{final} , $\sigma_{0.2\%}$, and σ_{LYP} are listed from which $\{\sigma_{\text{LYP}} - \sigma_0^{\text{final}}\}$ is derived. The σ_0^{final} ratio for IA-BH and IA is $117.21/451.43 = 0.259$, suggesting that the friction stress σ_0^{final} of IA-BH is primarily a result of the load-carrying component of martensite and $\{\sigma_{\text{LYP}} - \sigma_0^{\text{final}}\}$ is a result of dislocation pinning. Figure 4 graphically illustrates the trends indicated in Table II wherein $(\sigma_{\text{LYP}} - \sigma_0^{\text{final}})$ for prestrained specimens decreases with prestrain although the stored dislocation density increases. On the other hand, σ_0^{final} increases with prestrain indicating additional strengthening resulting from nanoparticles and Cottrell atmospheres around dislocations

Table II. Calculated dislocation densities from flow stresses at designated pre-strain of IA whereby $\Delta\tau = \{(\sigma @ \varepsilon) - \sigma_0^{\text{final}} \text{ of IA}\}/M$

Sample (%)	σ_0^{final} MPa	$\sigma_{0.2\% \varepsilon}$ MPa	σ_{LYP} MPa	YPE e %	Pre- ε	$\sigma @ \varepsilon$ MPa	$\Delta\tau$ MPa	$\rho \times 10^{14} \text{ m}^{-2}$	$\rho_t \times 10^{14} \text{ m}^{-2}$	$\rho_t^{\text{TEM}} \times 10^{14} \text{ m}^{-2}$
IA	451.4	496.9	–	–	0.0	–	–	–	–	0.96
IA-BH	117.2	–	567.0	2.13	0.0	–	–	–	–	–
2%-BH	183.6	–	622.1	3.11	0.0198	556.8	35.13	0.30	0.60	–
5%-BH	326.2	–	662.8	2.76	0.0485	625.1	57.90	0.818	1.64	2.40
10%-BH	455.5	–	687.0	2.63	0.0953	688.2	78.90	1.52	3.04	3.04

generated during the prestrain is taking place within the ferrite in addition to the load-carrying capacity of martensite.

DISCUSSION

The notable aspect of the as-quenched from 780°C specimen IA to that after BH at 175°C is the appearance of a distinct upper and lower yield point with a large YPE. Because the quenching process produced a dislocation density of about $0.96 \times 10^{14} \text{ m}^3$ in ferrite,¹⁴ it appears that the equilibrium carbon content in solution of ferrite at 780°C was distributed to sinks other than the dislocations newly formed to accommodate martensite formation, such as Fe_3C . If such were not the case, Cottrell atmosphere pinning at room temperature would have been evident. The sinks for the ejected carbon of the martensite forming regions have been attributed to its segregation to retained austenite.²⁶ Nevertheless, the APT results indicate that carbon content in the ferrite matrix free of any visible carbon segregation for IA is larger than that after BH.⁹ Hence, the carbon must exist in metastable clusters rather than in single solutes. The possible evidence of such an occurrence was discussed by Abe²⁷ who found that upon quenching Fe-C-Mn steels from about 700°C, Mn-C complexes formed in the ferrite but decomposed upon aging at 150°C to form ε -carbides. In the case of Fe-C alloys that were prestrained at 78 K after quenching from 900 K (627°C), Takaki et al.²⁸ attributed the resistivity recovery peak at 345 K (72°C) to carbon migration to monovacancy–carbon complexes and that at 365 K (92°C) to the formation of ε -carbide. They note that the presence of dislocations lowers the precipitation temperature of these carbides. Assuming these reactions are applicable in general to Mn-C steels, it is surmised that quenching of DP steel containing Mn produces both vacancy-carbon and Mn-C complexes, which account for the large σ_0^{final} of 451.4 MPa for IA versus 117.2 for IA-BH. The strengthening resulting from these clusters would be akin to that of solid solution hardening and would not give rise to a yield point, whereas upon dissolution followed by pinning of freshly formed dislocations upon BH, as a result of the

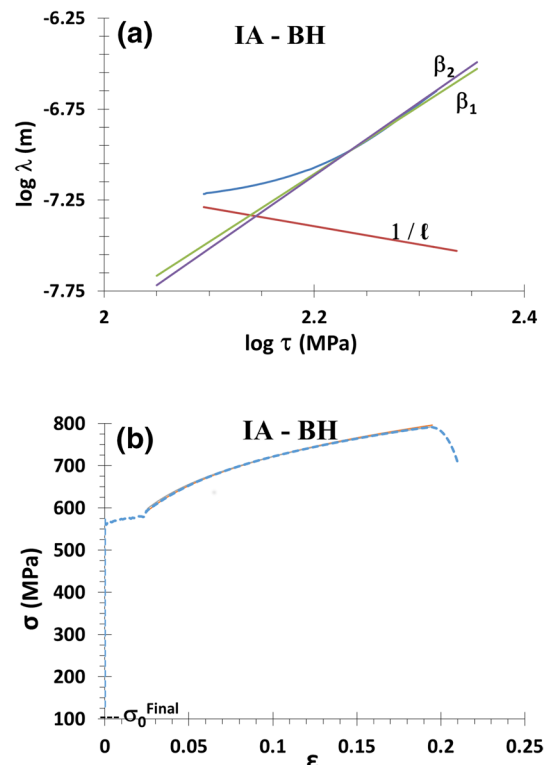


Fig. 2. (a) Log λ versus log τ for DP steel after bake hardening, IA-BH. (b) Stress–strain data set with fitted loci noting the position σ_0^{final} without displaying the extrapolated β_1 locus.

released carbon solutes, would do so. Nevertheless, ε -carbide precipitation within the polygonal ferrite seems to be absent until prestraining formed random forest dislocation density within the matrix because cells were not observed but Fe_3C were present. These forest dislocations acted as nuclei for carbide formation within the polygonal ferrite matrix giving rise to the increase in σ_0^{final} , as observed in Fig. 4. Moreover, if this increase in σ_0^{final} is attributed to the formation of ε -carbide, a reduction in free solute carbon to pin dislocations would result as indicated by the decline in $\{\sigma_{\text{LYP}} - \sigma_0^{\text{final}}\}$ with prestrain. Thus, the microstructure interpretation using CRA appears to correlate

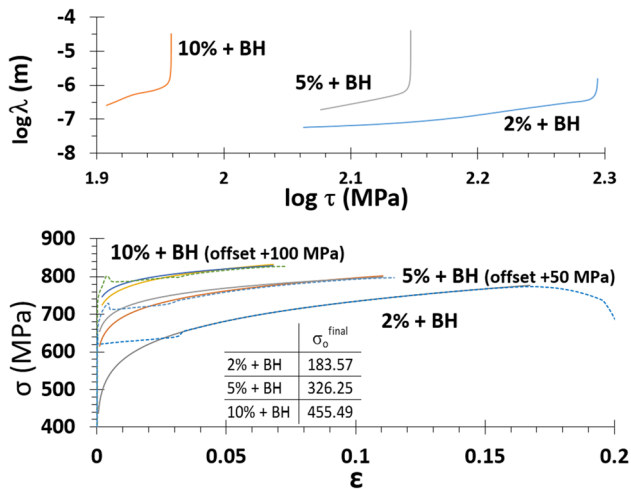


Fig. 3. Log λ versus log τ for all prestrain and bake-hardened specimens together with their fitted $\sigma - \varepsilon$ loci and the original data set (dashed). Note the offset of the curves.

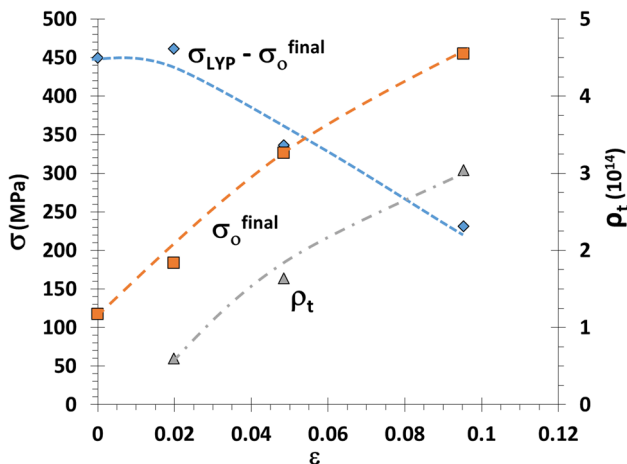


Fig. 4. σ_o^{final} and $\{\sigma_{\text{LYP}} - \sigma_o^{\text{final}}\}$ stresses from Table II versus true strain compared with the increase in dislocation density.

with the thermodynamic processes of formation of carbon complexes, its dissolution, and its formation of metastable carbides. Yet, the yield point effect may not be simply that of Cottrell-Bilby segregation of carbon solutes to dislocation cores. This well-documented process occurs at room temperature and is more or less complete at 30 min below 373 K (100°C).²⁹ Timokhina et al.¹⁴ noted TEM observation of identifiable carbides in dislocation cell walls as well as nanocarbides in the polygonal ferrite matrix after 10% prestrain followed by BH. Thus, the pinning of the dislocations may be attributed to nanocarbide precipitation on dislocation cores from carbon atmospheres via pipe diffusion, thus, enhancing the segregation effect of dislocations resulting in more efficient solute sinks. As pointed out by Timokhina et al.,¹⁵ APT cannot identify crystallographic structures, and hence their

observed carbon spots of about 1.0 nm may represent clusters or nanocarbides. Although high-resolution images can reveal atoms in distinct rows for well-defined precipitates unlike the case for clusters, extensive documentation is necessary. The self-consistent deductions are premised on the fact that σ_o^{final} determined as described actually defines the friction stress at which dislocations initially start to percolate through the polygonal ferrite matrix and give credence to its validity.

CONCLUSION

The application of the new constitutive relations analyses to dual-phase steel products shows that stress-strain loci reveal additional parameters that correlate to the TEM and APT observations. The prime new parameter is the determination of σ_o^{final} by back-extrapolation of the initial fit locus to define the stress at which dislocations would have initiated its percolation preyield process if the yield phenomenon were absent. This analysis separates the yielding from the post-YPE plastic processes, and σ_o^{final} defines the friction stress to generate heat upon dislocation movement. The shape-change component is hence a result of $\{\sigma - \sigma_o^{\text{final}}\}/M$ and is correlated to the mean slip distance λ . The evolving work-hardening mechanisms appear to rapidly change in the diffuse neck zone and correlate to the start microstructure. Thus, it is concluded that CRA is an improved method for materials testing analysis.

ACKNOWLEDGEMENTS

The authors thank the Natural Sciences and Engineering Research Council (Canada) and Australia Research Council for support of continued studies on crystal plasticity. We thank Mr. Jeffrey Handley for computational assistance.

ELECTRONIC SUPPLEMENTARY MATERIAL

The online version of this article (doi:10.1007/s11837-017-2339-1) contains supplementary material, which is available to authorized users.

REFERENCES

1. C.C. Tasan, M. Diehl, D. Yan, M. Bechtold, F. Roters, L. Schemmann, C. Zheng, N. Peranio, D. Ponge, M. Koyama, K. Tsuzaki, and D. Raabe, *Ann. Rev. Mater. Res.* 45, 391 (2015).
2. A.H. Nakagawa and G. Thomas, *Metall. Trans. A* 16A, 831 (1985).
3. M.S. Rashid, *Ann. Rev. Mater. Sci.* 11, 245 (1981).
4. J.H. Hollomon, *Trans. AIME.* 162, 268 (1945).
5. Y. Tomita and K. Okabayashi, *Metall. Trans. A* 16, 865 (1985).
6. A. Kumar, S.B. Singh, and K.K. Ray, *Mater. Sci. Eng., A* 474, 270 (2008).
7. J. Drillet, N. Valle, and T. Iung, *Metall. Mater. Trans. A* 43, 4947 (2012).

8. C.C. Tasan, M. Diehl, D. Yan, C. Zambaldi, P. Shanthraj, F. Roters, and D. Raabe, *Acta Mater.* 81, 386 (2014).
9. C.C. Tasan, J.P.M. Hoefnagels, M. Diehl, D. Yan, F. Roters, and D. Raabe, *Int. J. Plast* 63, 198 (2014).
10. S. Saimoto and P. Van Houtte, *Acta Mater.* 59, 602 (2011).
11. S. Saimoto and D.J. Lloyd, *Acta Mater.* 60, 6352 (2012).
12. S. Saimoto, O. Cazacu, and G.C. Kaschner, *Mater. Sci. Eng., A* 543, 129 (2012).
13. W. Thomson, *Philos. Trans. R. Soc. Lond.* 146, 649 (1856).
14. I.B. Timokhina, P.D. Hodgson, and E.V. Pereloma, *Metall. Mater. Trans. A* 38, 2442 (2007).
15. I.B. Timokhina, E.V. Pereloma, S.P. Ringer, R.K. Zheng, and P.D. Hodgson, *ISIJ Int* 50, 574 (2010).
16. S. Saimoto, *Philos. Mag.* 86, 4213 (2006).
17. G.I. Taylor, *J. Inst. Metals* 62, 307 (1938).
18. S. Saimoto, P. Van Houtte, K. Inal, and M.R. Langille, *Acta Mater.* 118, 109 (2016).
19. S. Saimoto and B.J. Diak, *Philos. Mag.* 92, 1890 (2012).
20. S. Saimoto, B.J. Diak, and D.J. Lloyd, *Philos. Mag.* 92, 1915 (2012).
21. S. Saimoto and B.J. Diak, *Mater. Sci. Eng., A* 322, 228 (2002).
22. M.F. Ashby, *Philos. Mag.* 21, 399 (1970).
23. J.H. Hollomon, *Trans. AIME.* 171, 535 (1947).
24. M. Delince, Y. Brechet, J.D. Embury, M.G.D. Geers, P.J. Jacques, and T. Pardoen, *Acta Mater.* 55, 2337 (2007).
25. A.J.E. Foreman and M.J. Makin, *Can. J. Phys.* 45, 5110 (1967).
26. F. Hu, K.M. Wu, and R.D.K. Mishra, *Mater. Sci. Tech.* 28, 1314 (2012).
27. H. Abe, *Scand. J. Metall.* 13, 226 (1984).
28. S. Takaki, T. Kimura, and H. Kimura, *Mater. Sci. Forum* 15, 691 (1987).
29. S. Harper, *Phys. Rev.* 83, 709 (1951).